

# Metasurface-Empowered Quantum Photonics

Yangwu Li, Wenwei Liu, Zhancheng Li, Hua Cheng,\* and Shuqi Chen\*

In recent decades, quantum information technologies have attracted significant attention and experienced rapid development due to their ultrafast processing speeds and high level of information security. A significant trend in this field of study involves the ongoing pursuit of integrating and miniaturizing quantum devices. Metasurfaces, which are artificially designed planar nanostructure arrays with versatile wavefront shaping capabilities, present a promising platform for the development of integrated photonic quantum devices by effectively controlling quantum light in multiple degrees of freedom. In this review, recent advances in the field of quantum photonics facilitated by metasurfaces, encompassing quantum light sources, manipulation and measurement of quantum states, and the intriguing functionalities of quantum metasurfaces, are summarized. Additionally, potential future directions for the advancement of quantum metasurfaces are discussed.

in a superposition state  $|\psi\rangle = \alpha|0\rangle + \beta|1\rangle$ , in which  $\alpha$  and  $\beta$  denote probability amplitudes. Such a qubit signifies both 0 and 1 concurrently, unlike classical bits which can only represent either 0 or 1, demonstrating the distinctive quantum parallelism of qubits. Besides, qubits can be entangled with one another in non-classical correlations. The presence of quantum entanglement and quantum parallelism enables quantum computing to be executed in a parallel fashion, leading to a notably heightened computational speed in comparison to classical computing, particularly when a substantial number of qubits are entangled. Moreover, due to the indivisibility of a single qubit and the no-cloning theorem of quantum states, the unauthorized interception and duplication of quantum states are fundamentally precluded in quantum information technology.

## 1. Introduction

Quantum information technologies, considered a major scientific advancement of the 20th century, have seen impressive progress in recent decades, especially in the fields of quantum communication, quantum computing, and quantum metrology. The fundamental unit of processing in this field is known as a qubit. In quantum mechanics, a qubit is encoded by two orthogonal states, which can be designated as  $|0\rangle$  and  $|1\rangle$  respectively. Different from the classical bit in computer science, a qubit can be


These inherent benefits of quantum information technologies render them highly auspicious for the advancement of next-generation information technology. A range of physical systems can be utilized to implement qubits, such as photons,<sup>[1]</sup> quantum dots (QDs),<sup>[2]</sup> trapped atoms,<sup>[3]</sup> nuclear magnetic resonance,<sup>[4]</sup> and superconducting circuits.<sup>[5]</sup> Among these systems, photons exhibit relatively weak coupling to their environment, allowing them to sustain favorable quantum coherence. Additionally, photons offer various dimensions for encoding qubits, including path, polarization, phase, frequency, spin angular momentum (SAM), and orbital angular momentum (OAM). Photonic qubits can be manipulated and transmitted effortlessly by ordinary optical elements, making them an ideal carrier of quantum information. Although traditional optical elements, such as waveplates, mirrors, and beam splitters et al. can fulfill the requirements for controlling photonic qubits in free-space applications, their large size, intricate alignment procedure, and limited mechanical durability make them incompatible with the ongoing trend of miniaturization and integration in quantum information systems. Fortunately, the rapid advancement of metasurfaces, a recently proposed type of compact photonic devices, has presented a pivotal breakthrough in addressing this dilemma.

In 2011, Yu and Capasso et al. formulated the generalized Snell's law and realized anomalous reflection and refraction by fabricating V-shaped gold antennas with spatially varying phase responses.<sup>[6]</sup> This breakthrough marked the beginning of metasurfaces, which are sophisticated artificial nanostructure arrays with subwavelength spatial resolutions. Over the past decade, metasurfaces have emerged as a research hotspot due to their excellent capabilities for the precise manipulation of light's amplitude, phase, and polarization.<sup>[7]</sup> The basic building

Y. Li, W. Liu, Z. Li, H. Cheng, S. Chen  
The Key Laboratory of Weak Light Nonlinear Photonics  
Ministry of Education  
School of Physics and TEDA Institute of Applied Physics  
Nankai University  
Tianjin 300071, China  
E-mail: hcheng@nankai.edu.cn; schen@nankai.edu.cn

S. Chen  
School of Materials Science and Engineering  
Smart Sensing Interdisciplinary Science Center  
Nankai University  
Tianjin 300350, China

S. Chen  
The Collaborative Innovation Center of Extreme Optics  
Shanxi University  
Taiyuan, Shanxi 030006, China

 The ORCID identification number(s) for the author(s) of this article can be found under <https://doi.org/10.1002/adpr.202300352>.

© 2024 The Authors. Advanced Photonics Research published by Wiley-VCH GmbH. This is an open access article under the terms of the Creative Commons Attribution License, which permits use, distribution and reproduction in any medium, provided the original work is properly cited.

DOI: 10.1002/adpr.202300352

blocks of metasurfaces are referred to as meta-atoms, which are subwavelength resonators typically made of dielectric or metallic materials. In contrast to conventional optical elements that manipulate light through accumulated phase changes along different optical paths, metasurfaces with ultrathin thicknesses shape the wavefronts of light by leveraging the localized resonant or nonresonant modes of electromagnetic fields in the meta-atoms. Despite the discrete nature of meta-atoms, the manipulation of light by metasurfaces can be regarded as quasicontinuous because of their subwavelength sizes. The physical principles governing phase control in metasurfaces can be classified into three categories: resonant phase,<sup>[8]</sup> propagation phase,<sup>[9]</sup> and geometric phase.<sup>[10]</sup> The resonant phase and propagation phase depend on the shape and size of meta-atoms, while the geometric phase is influenced by the spatial orientation of meta-atoms. Metasurfaces have been extensively employed to substitute conventional waveplates, lenses, gratings, holograms, and vortex beam generators due to their lightweight, ultracompact, integratable, robust, and multifunctional characteristics enabled by the unparalleled design flexibility of meta-atoms.<sup>[11]</sup> Especially in recent years, research on metasurfaces has expanded beyond the realm of classical optics, sparking growing interest in incorporating these versatile metasurfaces into the field of quantum photonics.

In this review, we provide a summary of the recent advances in metasurface-empowered quantum photonics. As depicted in **Figure 1**, notable progress has been made in three primary aspects, including quantum light sources, manipulation of quantum states, and unusual quantum functionalities. There are two kinds of metasurface-assisted quantum light sources: one is founded on quantum emitters (QEs) that generate single photons through spontaneous emission, while the other relies on nonlinear crystals that produce entangled photon pairs utilizing the process of spontaneous parametric downconversion (SPDC). The QEs integrated with metasurfaces or nanostructure antennas can be QDs,<sup>[12]</sup> 2D materials,<sup>[13]</sup> and color centers within nanodiamonds et al.<sup>[14]</sup> As for the photon-pair sources, the nonlinear crystal films are combined with dielectric metasurfaces<sup>[15]</sup> or directly molded into meta-atom arrays.<sup>[16]</sup> The manipulation of quantum states via metasurfaces primarily focuses on the distillation,<sup>[17]</sup> generation,<sup>[18]</sup> transformation, and distribution of quantum entangled states.<sup>[19]</sup> Metasurfaces can also be used to construct multiple projection bases to achieve the measurement of quantum states.<sup>[20]</sup> Moreover, metasurfaces are capable of achieving various intriguing functionalities, such as quantum imaging,<sup>[21]</sup> coherent perfect absorption of quantum light,<sup>[22]</sup> quantum sensing,<sup>[23]</sup> and quantum weak measurements.<sup>[24]</sup>

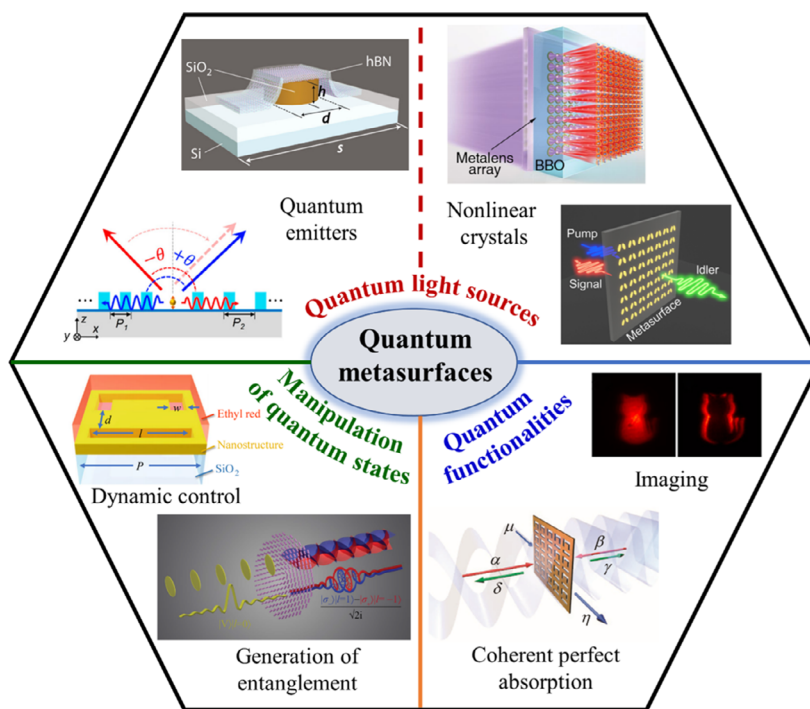


**Figure 1.** Metasurface-empowered quantum photonics. Schematic representation of the three major areas where metasurfaces can be utilized in quantum photonics, including quantum light sources (top), manipulation of quantum states (bottom left), and quantum functionalities (bottom right). Metasurface-assisted quantum light sources are classified into two categories: QEs for single photons (e.g., 2D materials<sup>[13]</sup> and color centers in diamonds,<sup>[14]</sup> top left) and nonlinear crystals for photon pairs (top right). Reproduced with permission.<sup>[13,14]</sup> Copyright 2020, American Chemical Society (ACS), and Copyright 2018, Optical Society of America (OSA). Nonlinear crystals can be combined with metasurfaces<sup>[15a]</sup> or directly fabricated into metasurfaces.<sup>[16b]</sup> Reproduced with permission.<sup>[15a]</sup> Copyright 2020, American Association for the Advancement of Science (AAAS). Reproduced under terms of the CC-BY license.<sup>[16b]</sup> Copyright 2023, The Authors, published by Royal Society of Chemistry (RSC). Metasurfaces are also harnessed to dynamically control quantum states<sup>[17b]</sup> and create entangled states.<sup>[18]</sup> Reproduced under terms of the CC-BY license.<sup>[17b]</sup> Copyright 2022, The Authors, published by Springer Nature. Reproduced with permission.<sup>[18]</sup> Copyright 2018, AAAS. The detection of quantum light enabled by metasurfaces allows for many novel functionalities, including imaging,<sup>[21]</sup> coherent perfect absorption,<sup>[22]</sup> et al. Reproduced under terms of the CC-BY license.<sup>[21]</sup> Copyright 2020, The Authors, published by AAAS. Reproduced under terms of the CC-BY license.<sup>[22]</sup> Copyright 2015, The Authors, published by Springer Nature.

## 2. Quantum Light Sources

Quantum light sources are essential components of quantum information technologies, producing individual photons that serve as carriers of qubits. The single-photon emitters (SPEs) and SPDC photon-pair sources are two of the most readily accessible quantum light sources in laboratory settings. The former contains single atoms,<sup>[25]</sup> single-dye molecules,<sup>[26]</sup> QDs,<sup>[27]</sup> defects in 2D materials,<sup>[28]</sup> and color centers in diamonds et al.<sup>[29]</sup> SPEs can transition from the ground state to the excited state when stimulated by pump waves, followed by a spontaneous return to the ground state accompanied by the emission of a photon. Generally speaking, there are three essential factors to evaluate the performance of a SPE: the indistinguishability of generated photons, unicity, and emission efficiency. The concept of indistinguishability implies that all produced photons share the same quantum states and carry identical quantum information. The unicity requires that the source emits no more than one photon during a specified clock cycle, which excludes the possibility of two photons arriving at the detectors simultaneously, a phenomenon known as photon antibunching.<sup>[30]</sup> This single-photon emission characteristic is typically evaluated through a Hanbury Brown–Twiss experiment to measure the second-order correlation function  $g^{(2)}(t)$  of photons emitted from the SPE.<sup>[31]</sup> Generally speaking, a light source with  $g^{(2)}(0) < 0.5$  can be identified as a SPE. In contrast, the emission of photon pairs from nonlinear crystals is enabled by the process of SPDC, in

which a single photon from the pump wave splits into two highly correlated daughter photons known as signal and idler photons. The signal and idler photons born at the same time and their momenta and frequencies are correlated by the phase-matching condition and energy conservation, respectively. Regrettably, both spontaneous emission and SPDC process exhibit inherent inefficiency. To address this issue, various metasurfaces have been proposed to efficiently collect emitted photons or induce resonances to amplify the local electromagnetic field in the vicinity of the QEs for facilitating the spontaneous emission in quantum light sources.<sup>[32]</sup>

### 2.1. SPEs Integrated with Metasurfaces

It is well known that the emission characteristics of SPEs can be approximated to those of electric dipoles. In other words, photons emitted from the free-standing emitters are radiated in all directions, which seriously impedes their collection and collimation. One feasible solution is demonstrated in **Figure 2a**.<sup>[33]</sup> A monolithic immersion metalens, composed of nanopillars, is etched onto the surface of a diamond substrate that contains a nitrogen-vacancy (NV) center located about 20  $\mu\text{m}$  underneath the surface. The presence of the metalens can effectively suppress the refraction and reflection caused by the air/diamond interface. Taking advantage of the high refractive index of the diamond substrate, this ingenious design utilizes the diamond substrate as an immersion medium for the metalens,

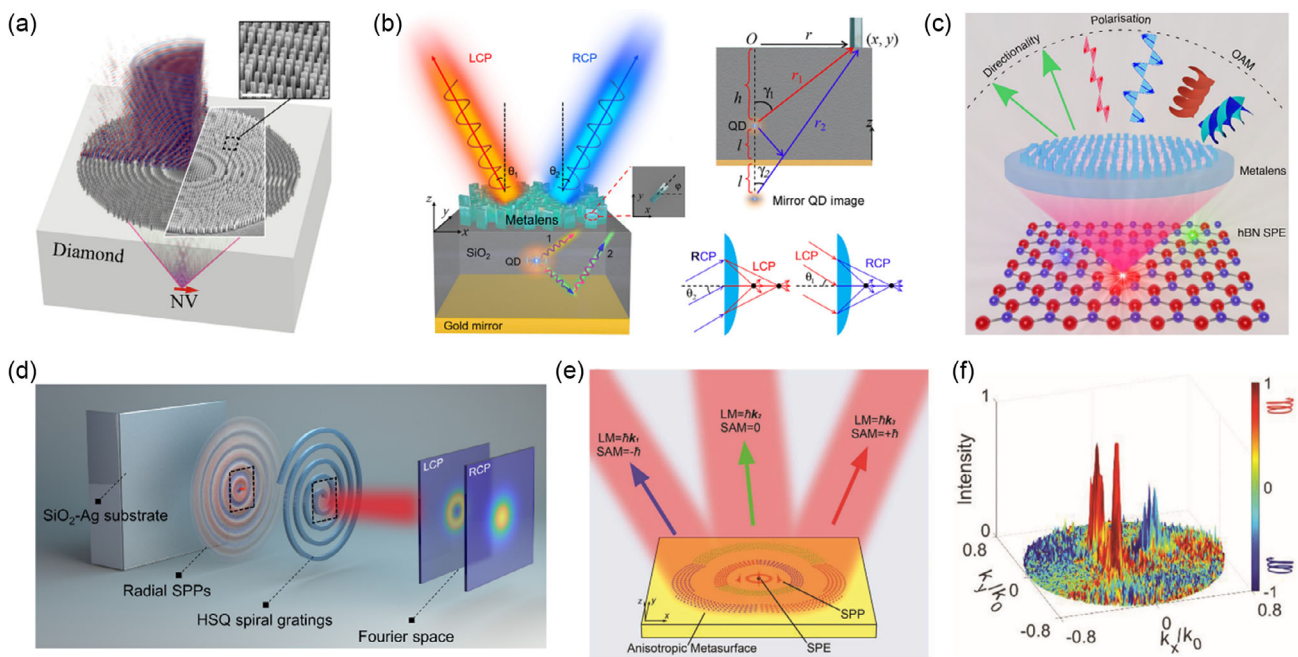


**Figure 2.** SPEs integrated with metasurfaces. a) Monolithic immersion metalens for enhancing single-photon collection and collimation of an NV center. Reproduced under terms of the CC–BY license.<sup>[33]</sup> Copyright 2019, The Authors, published by Springer Nature. b) Bifocal metalens for spin-state splitting and enhancement of single-photon emission. Reproduced under terms of the CC–BY license.<sup>[27]</sup> Copyright 2020, The Authors, published by AAAS. c) Metasurface-enabled structuring of single-photon emission in multiple DOFs. Reproduced under terms of the CC–BY license.<sup>[34]</sup> Copyright 2023, The Authors, published by Springer. d) OAM-encoded SPE based on photon–plasmon–photon conversion process. Reproduced under terms of the CC–BY license.<sup>[29]</sup> Copyright 2022, The Authors, published by AAAS. e) Multichannel SPE with free controls of independent SAMs and LMs. f) Measured 3D scattered field intensity distributions of the proposed multichannel SPE in e). (e,f) Reproduced with permission.<sup>[12]</sup> Copyright 2023, Wiley-VCH GmbH.

contributing to a high numerical aperture (NA:  $\approx 1.0$ ) of the metalens. As a result, the metalens not only allows for imaging of the NV center but also facilitates efficient collection and collimation of its emission. Likewise, Bao et al. proposed a spin-splitting bifocal metalens to manipulate the spin state of single photons emitted from a QD.<sup>[27]</sup> Compared to the last design, this metalens has an additional attractive function: it can split the single-photon emission into two arbitrary directions with opposite spin states. As shown in Figure 2b, a QD is embedded in the middle dielectric layer within a metal–dielectric–metalens structure, where the metal layer operates as a mirror to reflect the downward propagating photons. The splitting of spin states is achieved by a geometric phase metasurface. The emission from the QD with random polarization can be decomposed to right and left circular polarizations (RCP and LCP). Therefore, when the RCP and LCP components pass through the metasurface, they are converted to the opposite circular polarizations and emitted in two desired directions (denoted by  $\theta_1$  and  $\theta_2$  shown in the inset). The total energy emitted by the QD has four dissipative channels: upward scattering through the metasurface, scattering along the dielectric layer, absorption by the metasurface, and absorption by the metal layer. Since only the first term contributes to the desired single-photon beam, the photon collection efficiency of this source is defined as the proportion of the energy of the first channel in the total energy. To maximize the photon collection efficiency, the positions of both the QD and its mirror image are precisely aligned with two focal points of the metalens. Compared to a structure with only a metasurface and no metal mirror, the peak intensity of far-field scattered light in a complete structure is doubled. Thus, the introduction of the metal mirror significantly enhances the collection of QD emissions, resulting in a 32% collection efficiency. This method allows for the simultaneous manipulation of single-photon emission in two degrees of freedom (DOFs)—SAM and path. Lately, the manipulated DOFs of single-photon emission have been further extended to include polarization and OAM.<sup>[34]</sup> The highest DOFs yet in manipulating single-photon emission have been achieved by a multifunctional metalens based on the propagation phase principle. As shown in Figure 2c, the metalens is composed of cuboid-shaped meta-atoms arranged in a square lattice. The individual meta-atom with a fixed height operates as a truncated rectangular waveguide, and its birefringence property can be adjusted by varying its transverse sizes. Consequently, independent wavefronts can be encoded in two orthogonal polarized components of the hBN single-photon emission. By combining the phase profiles of a polarization-selective grating and a lens into one metasurface, the single-photon emission can be collected and split into two directions with orthogonal linear polarizations. Furthermore, substituting the phase profile of the polarization-selective grating with that of a vortex grating results in the generation of distinct OAM modes with orthogonal polarizations in two emission channels.

Another configuration is to place the metasurfaces on the same plane as the SPEs, which is typically associated with the excitation of surface plasmon polaritons (SPPs). Figure 2d depicts a layer-by-layer representation of an OAM-encoded SPE, which consists of a SiO<sub>2</sub>-coated Ag substrate and a spiral grating containing a centrally located NV center.<sup>[29]</sup> The NV center is carefully selected through luminescence measurements to

ensure that its transition dipole is normal to the substrate surface for maximizing the single-photon emission efficiency. Once the selected NV center is pumped by a tightly focused radially polarized laser beam, the resulting single-photon emission will excite radially diverging SPPs supported by the air–SiO<sub>2</sub>–Ag interface. After propagating over azimuthally varied distances, the SPPs are outcoupled by the Archimedean spiral grating as well-collimated single photons. Based on numerical analysis, the far-field polarization state of generated single photons can be denoted by  $|\psi_m\rangle = (|R\rangle|m+1\rangle - |L\rangle|m-1\rangle)/\sqrt{2}$ , where  $m$  is the arm number of the Archimedean spiral grating,  $|R\rangle$  and  $|L\rangle$  represent the RCP and LCP states,  $|m\rangle$  represents the OAM state with a topological charge of  $m$ . Obviously, this study clearly demonstrates a practical method for producing well-collimated single photons carrying SAM–OAM entangled states. For the designed one-armed OAM-encoded SPE, the simulation results reveal that 78.4% of the total single photons produced by the source are transformed into SPPs. Only 38.2% of these SPPs are scattered by the spiral grating to produce the desired vortex beam, while the rest is either absorbed or continues as SPPs. In addition, Jia et al. proposed an alternative metasurface for outcoupling the SPPs excited by the emitted single photons from a CdSe QD, as shown in Figure 2e.<sup>[12]</sup> The basic nanoscatteer consists of two identical nanogrooves etched into the metal film. By adjusting the orientations and radial distance of two nanogrooves, their respective scattered linearly polarized (LP) lights can be superposed into arbitrary polarization states, including circular polarizations. The nanoscatteers are arranged to manipulate the emission directions (corresponding to linear momentums, LMs) based on the constructive interference condition of the scattered field. Figure 2f shows the experimental far-field scattered light distribution from a clover-shaped metasurface designed using the aforementioned principle, with the color indicating the chirality. The SAM-encoded single photons exhibit three emission directions, with two of them being filled by single photons in LCP (SAM =  $+\hbar$ ) and the remaining direction being filled by single photons in RCP (SAM =  $-\hbar$ ). Compared to the SPE-metalens configurations depicted in Figure 2a–c, the final two schemes may demonstrate reduced emission efficiency as a result of unavoidable Joule losses in plasmonic metasurfaces. Nevertheless, the coplanar positioning of the SPE and metasurface streamlines their alignment and fabrication procedures following the selection and marking of the SPE. Furthermore, it should be emphasized that all the measured  $g^{(2)}(0)$  of SPEs discussed above is significantly less than 0.5, indicating that the single-photon emission characteristics of SPEs are well preserved after integration with the metasurfaces.

## 2.2. SPDC Photon-Pair Sources

One straightforward approach to enhance the probabilistic emission of photon-pair is to employ nonlinear crystals with high second-order susceptibilities  $\chi^{(2)}$ , which plays a crucial role in the SPDC process. However, the miniaturization of photon-pair sources involves a tradeoff between compactness and the generation rate of photon pairs, as a result of the decreased volume of nonlinear crystals. From the perspective of quantum mechanics, the spontaneous transition of a quantum light source

is stimulated by the quantum vacuum field, and the transition probability scales with the density of states. By inducing various resonances in metasurfaces to increase the density of states, one can strengthen the quantum vacuum field and thus facilitate the SPDC process.<sup>[35]</sup>

For example, Santiago-Cruz et al. proposed leveraging the Mie-like resonance in the lithium niobate (LN, with a high  $\chi^{(2)}$ ) metasurface to boost the SPDC process.<sup>[16a]</sup> As shown in **Figure 3a**, the metasurface is composed of truncated pyramids etched from a LN film on a transparent substrate. The pump laser is injected from the substrate side, and the photon pairs are collected in a reflective manner. The results show a 130-fold enhancement in photon-pair generation compared to the unpatterned LN film, attributed to the electric resonance in the LN metasurface. Besides, the spectrum of the emitted photon pairs can be effectively tuned by controlling the detuning wavelength between the electric resonance and SPDC degenerate wavelength. Son et al. designed a GaP metasurface that supports a quasi-bound state in the continuum (quasi-BIC) resonance to enhance photon-pair generation and split the single and idler photons in opposite directions.<sup>[16b]</sup> As shown in **Figure 3b**, the basic unit of the metasurface consists of two elliptical nanocylinders. Tilting two ellipses with respect to each other leads to the emergence of a high-Q-factor quasi-BIC resonance within the metasurface, resulting in a net in-plane electric dipole and opening a leaky channel for photon-pair emission. Due to the amplified density of states at the resonance wavelength, the photon-pair generation rate of the metasurface is significantly enhanced by a factor of 67 compared to that of an unetched

GaP film with the same thickness. The emission directivities of the signal and idler photons are further investigated using the experimental setup depicted in **Figure 3c**. By connecting ports A and E to individual single-photon detectors, the forward-backward emission geometry (one photon is emitted forward and the other is emitted backward) is studied. For the two unidirectional cases (forward-forward and backward-backward), a fiber splitter is used to separate the photon pairs into two single-photon detectors. According to the coincidence counts obtained from three emission geometries, it is determined that the majority (56%) of the generated photon pairs prefer to be emitted bidirectionally. This is an intriguing phenomenon that has never been observed before in metasurface-based SPDC sources. Furthermore, the use of nonlocal guided-mode resonances leads to a significantly higher spectral brightness of emitted photon pairs compared to the previously mentioned localized resonances.<sup>[15b]</sup> **Figure 3d** shows the sketch of the proposed photon-pair source, which features a thin LN film coated with a silica metagrating. The proposed design eliminates the need for an etching process on the LN film and ensures the preservation of its total volume. The electric field intensity in the LN film is significantly enhanced due to the metagrating-supported guided-mode resonances, effectively promoting the transverse phase matching of the SPDC process. Meanwhile, the longitudinal phase matching condition is relaxed because of the subwavelength thickness of the LN film.<sup>[36]</sup> It should be noted that in other metasurface-based SPDC photon-pair sources characterized by subwavelength thicknesses, the requirement for longitudinal phase matching can also be alleviated by exploiting the

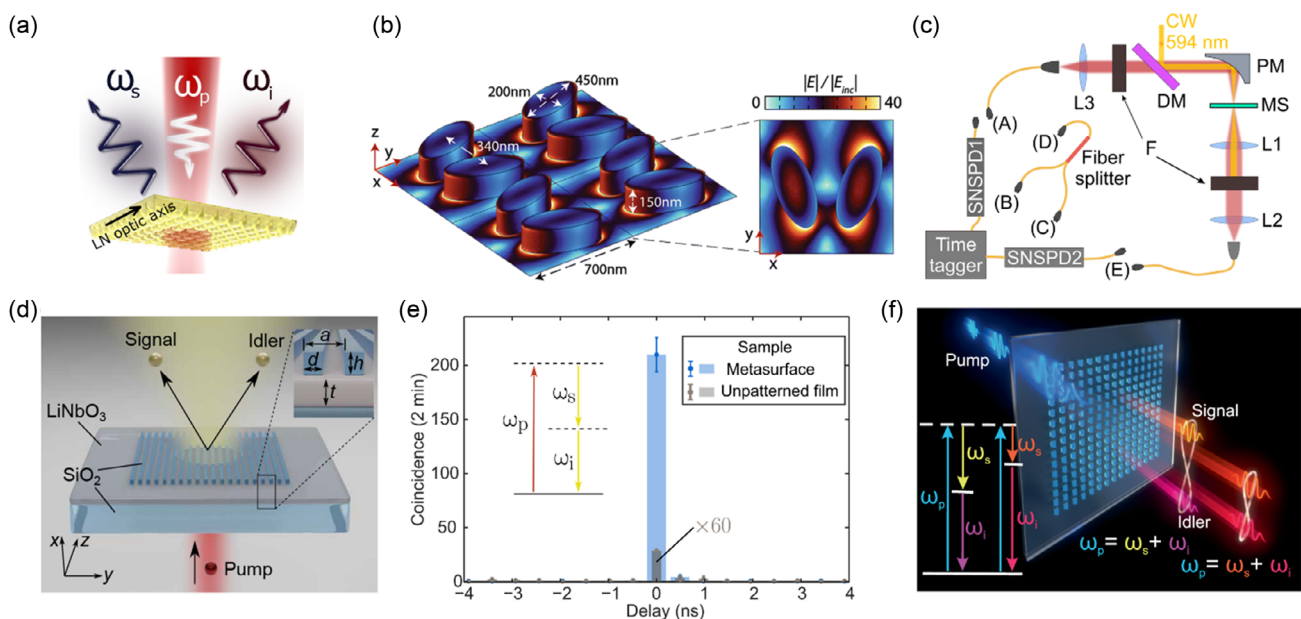


**Figure 3.** Metasurface-based SPDC photon-pair sources. a) Reflective nonlinear metasurface for enhancing photon-pair emission via Mie-like resonances. Reproduced under terms of the CC-BY license.<sup>[16a]</sup> Copyright 2021, The Authors, published by ACS. b) Bidirectional emission of photon pairs from a resonant nonlinear metasurface. c) The experimental setup for examining the bidirectionality in (b). (b,c) Reproduced under terms of the CC-BY license.<sup>[16b]</sup> Copyright 2023, The Authors, published by Royal Society of Chemistry (RSC). d) Photon-pair emission enhancement leveraging the nonlocal resonance in a LN nanofilm incorporated with a dielectric metagrating. e) Coincidence histograms of SPDC photon pairs from the sources in (d) and an unpatterned LN film with the same thickness. (d,e) Reproduced under terms of the CC-BY license.<sup>[15b]</sup> Copyright 2020, The Authors, published by AAAS. f) Nonlinear metasurface supporting quasi-BIC resonance for generating complex quantum states. Reproduced with permission.<sup>[16c]</sup> Copyright 2022, AAAS.

position–momentum uncertainty relation of the generated photons.<sup>[37]</sup> The coincidence counts of the SPDC photon pairs depicted in Figure 3e manifest a 450-fold enhancement in the photon-pair generation rate. In addition to facilitating the SPDC process, metasurface-supported resonances also have the capability to regulate the SPDC spectrum, especially in terms of their potential for creating complex quantum states. Santiago-Cruz et al. demonstrated that a carefully designed GaAs metasurface possessing a high  $\chi^{(2)}$  has significant potential in quantum state engineering.<sup>[16c]</sup> As shown in Figure 3f, the metasurface is composed of GaAs nanoblocks arranged in a square lattice. Each nanoblock is designed as a cube with a small notch to introduce structural asymmetry for exciting high-Q-factor quasi-BIC resonance in the metasurface. Due to the enhancement of the quantum vacuum field induced by the high-Q-factor resonance, the SPDC efficiency is three orders of magnitude higher than that in a GaAs film of the same thickness. It's found that altering the wavelength and polarization of the pump laser, or the spectral location of the resonances, results in the generation of frequency-degenerate and nondegenerate narrowband photon pairs without significant efficiency fluctuations. Moreover, by exploiting the single resonance or multiple resonances in a uniform or multipatch metasurface, it is possible to generate nondegenerate photon pairs at multiple frequencies, bringing forth complex quantum states, including cluster states. These findings reveal a novel nanoscale quantum source for generating complex entangled states, which is promising for facilitating the miniaturization of quantum information processing.

**Table 1** provides a clear and intuitive comparison of the variances in the operational mechanisms and performance of the photon-pair sources depicted in Figure 3. The photon-pair generation rate, a critical performance metric, is determined by dividing the coincident photon pair counts per unit time by the power of the pump light. Although the generation rates are low due to the subwavelength thickness of the metasurface-based sources compared to bulk sources, the resonance enhancement effect ensures that the generation rates remain significant. In general, integrating metasurfaces with photon-pair sources conforms to the miniaturization trends in quantum optics and opens up new possibilities for enhancing emission efficiency and directing photon streams by leveraging a range of resonances supported by metasurfaces.

### 2.3. Quantum Vacuum Engineering Dictated by Metasurfaces

Additionally, metasurfaces can be exploited to create an anisotropic quantum vacuum (AQV) for regulating the spontaneous radiation characteristics of multilevel QEs over a macroscopic distance. This regulation is the consequence of quantum

interference among different radiative decay channels of a QE with nearly degenerate excited states. In an isotropic quantum vacuum, quantum interference strictly requires nonorthogonal transition dipole moments, which is difficult to achieve for atomic QEs.<sup>[38]</sup> To overcome this constraint, researchers have proposed several theoretical methods for creating an AQV near an atomic QE for achieving quantum interference with orthogonal transition dipole moments, such as putting a multilevel atom in a multilayer dielectric medium<sup>[39]</sup> or near-metallic nanostructures.<sup>[40]</sup> In all of these efforts, the precise control and addressing of multilevel atoms in the near field of optical nanostructures pose significant challenges. Metasurfaces with remarkable ability of phase control offer realistic opportunities for engineering the quantum vacuum over macroscopic distances.<sup>[41]</sup> As shown in **Figure 4a**, Jha et al. designed a polarization-dependent plasmonic metasurface to create an AQV near the atomic QE situated in the far field. The QE is a three-level atom in a *V* configuration with two degenerate excited states  $|a_1\rangle$  and  $|a_2\rangle$  and one ground state  $|b\rangle$ . As shown in Figure 4b, the incident  $\gamma$ -*z* polarized light experiences mirror reflection at the metasurface, while the incident *x*-polarized light is reflected back to the source. When placing a two-level QE with in-plane (*x*-*y* plane) transition dipole at the focal point of the metasurface, the calculated radiative decay rate varies distinctly with the orientation of dipole, which verifies the presence of AQV over a long distance from the metasurface. It should be noted that the focal length of the metasurface is much larger than the wavelength. When replacing the two-level atom with a three-level atom, quantum interference between two orthogonal transitions ( $|a_1\rangle \rightarrow |b\rangle$  and  $|a_2\rangle \rightarrow |b\rangle$ ) emerges, resulting in abnormal excited state populations. As plotted in Figure 4c, the population of the excited state  $|a_1\rangle$  decays exponentially and the population of state  $|a_2\rangle$  remains at 0 when the atom is placed in an isotropic quantum vacuum. In contrast, with the metasurface-engineered AQV, the decay of the state  $|a_1\rangle$  population slows down, and the population of the state  $|a_2\rangle$  becomes nonzero. These findings indicate that metasurfaces can serve as an unexpected tool to regulate the radiation characteristics of atomic QEs based on the AQV-induced quantum interference.

Analogously, the metasurface-engineered AQV can further be exploited to realize the exciton valley coherence in transition metal dichalcogenide (TMDC) monolayers.<sup>[42]</sup> It is known that the TMDC monolayers possess direct bandgaps located at the energy-degenerate *K* and *K'* valleys at the corners of the hexagonal Brillouin zone.<sup>[43]</sup> As a long-sought goal in valleytronics, the coherent manipulation of excitons (Coulomb-bound electron–hole pairs) in *K* and *K'* valleys has been vastly researched, because it may provide a new dimension for quantum information encoding and processing, namely valley degree of freedom. However, due to the valley-dependent optical selection rule of

**Table 1.** Comparison of the photon-pair generation rates of the SPDC photon-pair sources illustrated in Figure 3.

References	Material	Resonance	Photon-pair wavelength [nm]	Thickness [nm]	Rate [mHz mW <sup>-1</sup> ]	Enhancement
[15b]	LiNbO <sub>3</sub>	Guided-mode	≈1570	304	21	450
[16a]	LiNbO <sub>3</sub>	Mie-like	≈1576	680	77	130
[16b]	GaP	Quasi-BIC	≈1188	150	3.4	67
[16c]	GaAs	Quasi-BIC	1446.8	320	8	>10 <sup>3</sup>

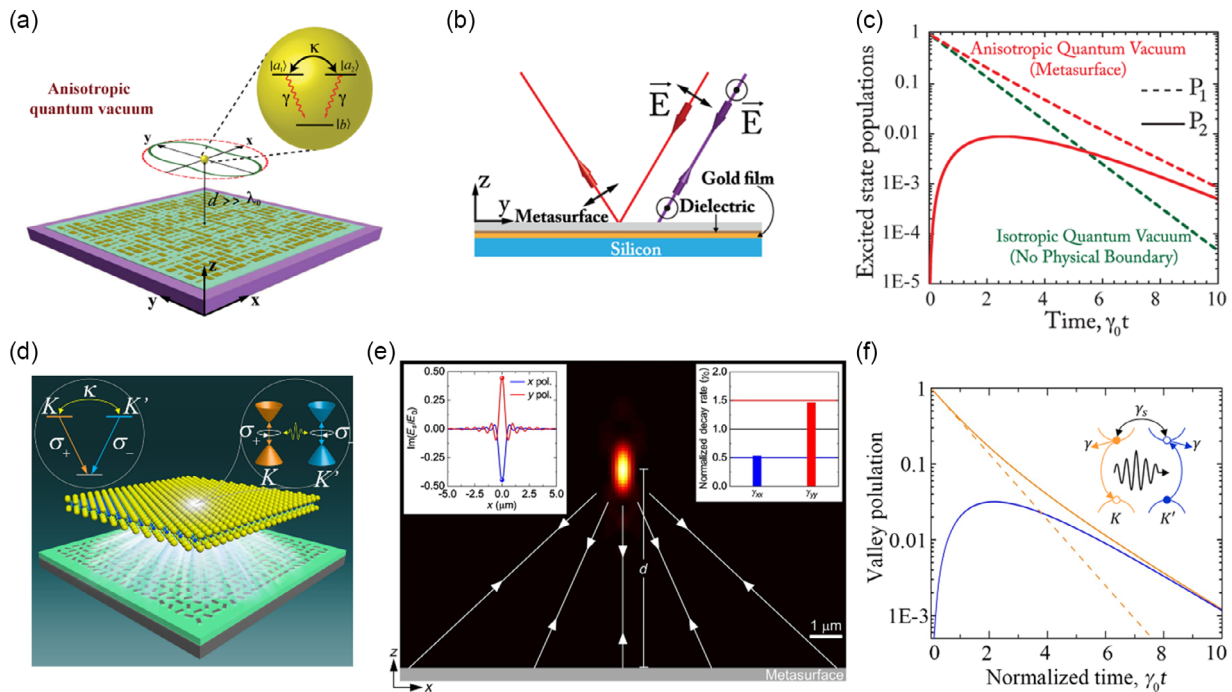


**Figure 4.** Far-field AQV-induced quantum interference based on metasurfaces. a) Schematic illustration of metasurface-enabled macroscopic quantum vacuum engineering. b) Polarization-dependent response of the metasurface proposed in (a). c) Population evolution of excited states of a three-level atom with normalized time  $\gamma_0 t$ . (a–c) Reproduced with permission.<sup>[41]</sup> Copyright 2015, American Physical Society (APS). d) Spontaneous generation of valley coherence in TMDC monolayer enabled by a metasurface-engineered AQV. e) Simulated scattered field intensity distribution of x-polarized excitonic dipole, where the metasurface is represented by bottom gray zone. The left inset shows the nondegenerate imaginary part of scattered field for x- and y-polarized dipoles. The right inset depicts the normalized decay rates for x- ( $\gamma_{xx}$ ) and y-polarized dipoles ( $\gamma_{yy}$ ). f) Population evolution of excitons in K and K' valleys with normalized time  $\gamma_0 t$ , with (solid lines) and without (dashed line) a metasurface-engineered AQV. (d–f) Reproduced with permission.<sup>[42]</sup> Copyright 2018, APS.

excitons in TMDC monolayers, the interband transition of excitons in the K (K') valley can only be excited by LCP (RCP) photons.<sup>[44]</sup> Thus, the interband transition in the K valley emitting LCP photons cannot excite the exciton transition in the orthogonal K' valley, making the coherence of excitons between the K and K' valleys naturally impossible in free space. To tackle this issue, Jha et al. innovatively proposed using a polarization-dependent metasurface to achieve exciton intervalley coherence in TMDC monolayers, as shown in Figure 4d. The electron–hole pairs in degenerate valleys in a TMDC monolayer can be modeled as an in-plane excitonic circularly polarized dipole with a V-shaped energy-level configuration. The geometric phase metasurface is designed to refocus the emission of the excitonic dipole to its origin for both x- and y-polarized dipoles (refer to Figure 4e). The imaginary part of the scattered field is enhanced, while the real part is suppressed. It can be seen from the insets in Figure 4e that such a design minimizes the imaginary part of the scattered field for an x-polarized dipole (maximizes for a y-polarized dipole) at the dipole position, resulting in an engineered AQV represented by two unequal normalized decay rates  $\gamma_{xx}$  (0.53) and  $\gamma_{yy}$  (1.47). The AQV-mediated coupling parameter  $\kappa$ , which describes the coupling between two orthogonal transitions in K and K' valleys (as shown in the inset of Figure 4d), is given by  $\kappa = (\gamma_{xx} - \gamma_{yy})/2$ . Only when  $\kappa$  is nonzero does the exciton intervalley coherence emerge. The calculated exciton

populations in different valleys are plotted in Figure 4f. Clearly, the situations are quite similar to those in Figure 4c. In free space, the population of K valley excitons (dashed line) decays exponentially, while K' valley excitons do not appear. When the TMDC monolayer is placed in an AQV, the population decay of K valley excitons is suppressed. The K' valley excitons initially increase and then decrease slowly (solid lines), indicating the generation of exciton intervalley coherence. Other than the previously reported schemes that require external coherent fields,<sup>[45]</sup> the metasurface-based AQV breaks the limit of valley-dependent optical selection rules and may promote the development of novel valleytronic devices.

### 3. Manipulation and Measurement of Photonic Quantum States

As the heart of quantum information processing, coherent manipulation of quantum states is indispensable for implementing quantum logic gates and quantum algorithms. Typically, these manipulations are performed on entangled states. When considering the manipulation of entangled states, a primary concern arises regarding whether the metasurface will disrupt the quantum entanglement. To figure this out, Altewischer et al. placed two perforated plasmonic metasurfaces separately on

two paths of entangled photon pairs and detected the transmitted photons.<sup>[46]</sup> According to the two-photon coincidence counting measurement, it was first demonstrated that entanglement can survive in the interaction between photons and metasurfaces, even in the presence of significant metallic loss. Henceforth, the exploration of metasurfaces for quantum state manipulation has expanded beyond plasmonic and dielectric metasurfaces<sup>[17a,18,20b,47]</sup> to include composite nonlinear metasurfaces.<sup>[17b]</sup>

For instance, Zhang et al. designed a composite nonlinear metasurface, as shown in the inset of Figure 1 (labeled “dynamic control”), to achieve all-optical control and distillation of quantum states.<sup>[17b]</sup> The metallic split ring slit array is coated with a polymer film containing ethyl red, a type of nonlinear photoisomeric material. Under the illumination of a control laser, the

molecular chains of ethyl red fold, resulting in a reversible decrease in the refractive index of the polymer film and further tuning the plasmonic resonance of the metasurface. Thus, the anisotropic responses of the nonlinear metasurface, such as the transmission efficiencies and phase delay of orthogonally polarized photons, can be efficiently tuned by optically switching the ethyl red between its two isomeric states. **Figure 5a** shows the conceptual scheme for dynamically controlling entangled states using the nonlinear metasurface. A polarization-entangled two-photon state is achieved by pumping a pair of SPDC crystals stacked with their optical axes being orthogonal to each other. The entanglement is intentionally reduced by inserting a birefringent crystal in the path of the signal photon. The signal photon is then sent to pass through the nonlinear metasurface, while the idler photon is directly detected to herald the

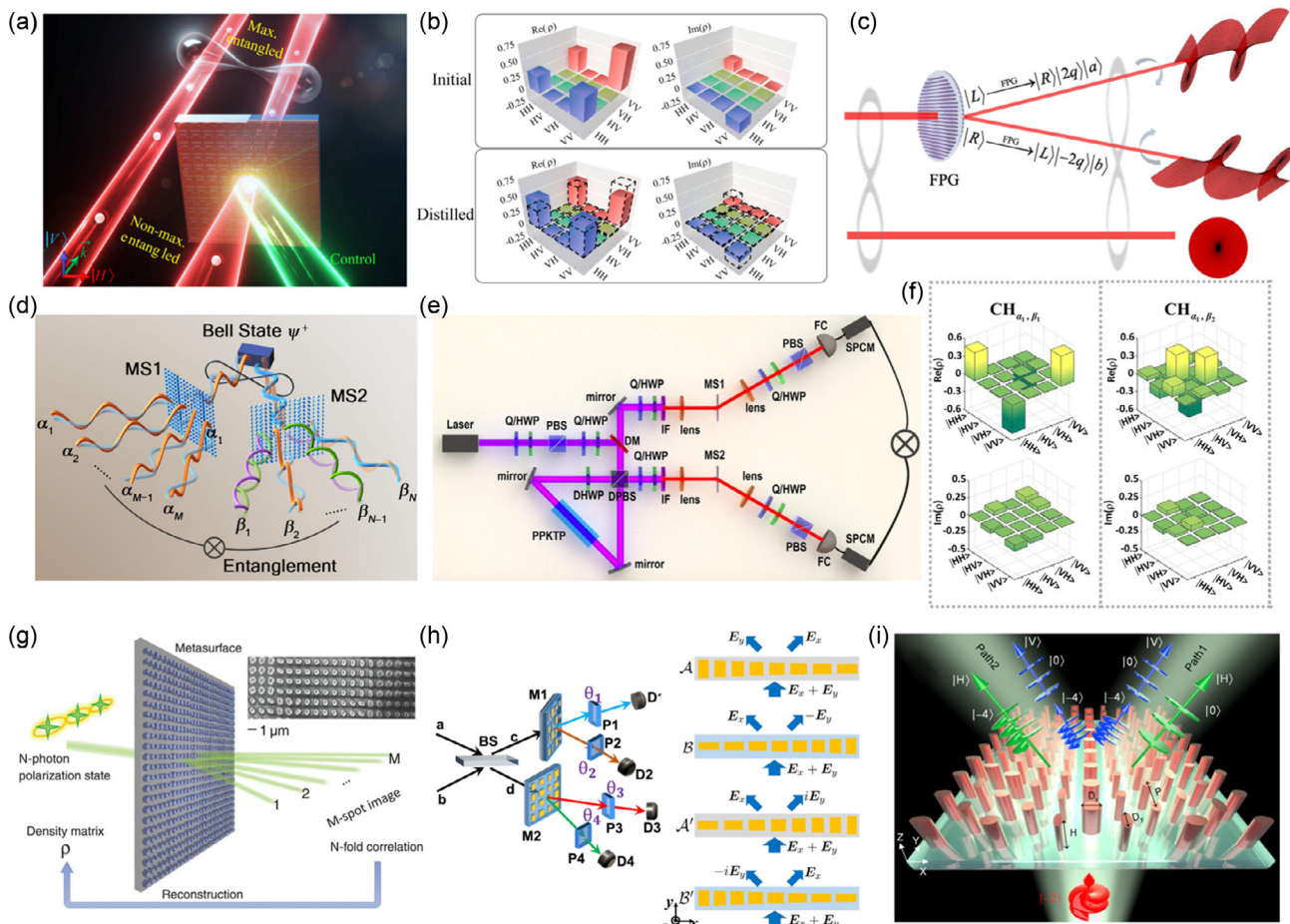


**Figure 5.** Manipulation and measurement of quantum states assisted by metasurfaces. a) All-optical control of quantum entangled states by a composite nonlinear metasurface. b) The density matrices of the initial nonmaximally entangled state and distilled maximally entangled state after applying control light on the metasurface. (a,b) Reproduced under terms of the CC-BY license.<sup>[17b]</sup> Copyright 2022, The Authors, published by Springer Nature. c) Generation of high-dimensional entanglement through the geometric phase metasurface-induced spin-orbital interaction. Reproduced with permission.<sup>[49]</sup> Copyright 2022, OSA. d) Entanglement distribution and transformation via two GSI metasurfaces. e) Experimental setup for verifying the generation of  $M \times N$  distributed entangled states. f) The reconstructed density matrices of two output states obtained from the designed  $2 \times 2$  entanglement distributor. (d–f) Reproduced with permission.<sup>[19]</sup> Copyright 2022, APS. g) Multiphoton polarization quantum state measurement using dielectric metasurface composed of multiple interleaved metagratings. Reproduced with permission.<sup>[20a]</sup> Copyright 2018, AAAS. h) Binary-pixel metasurface enabled complete measurement of polarization Bell state. The right panel showcases the two supercells of each metasurface and their functions. Reproduced under terms of the CC-BY license.<sup>[20b]</sup> Copyright 2023, The Authors, published by De Gruyter. i) Multiplexing metasurface for the measurement of single-photon OAM states. Reproduced with permission.<sup>[20c]</sup> Copyright 2023, ACS.



presence of the signal photon. By performing quantum state tomography,<sup>[48]</sup> Figure 5b shows the measured density matrix  $\rho$  of the entangled two-photon state with (upper panel) and without (lower panel) irradiating a control light onto the nonlinear metasurface. The initial unbalanced four corner elements in the real part of  $\rho$  become more balanced, and the original non-zero two antidiagonal elements in the imaginary part of  $\rho$  approach zero. In other words, the nonmaximally entangled state is almost restored to a Bell state, which has the highest degree of entanglement, confirming the entanglement distillation enabled by the optically switched nonlinear metasurface. This discovery provides valuable guidance for solving quantum state degradation caused by decoherence and dissipation in practical quantum systems.

It's worth noting that quantum entanglement exists not only between photon pairs generated in SPDC, but also between different DOFs of a single photon.<sup>[18]</sup> For instance, a geometric phase metasurface is devised to mimic the action of a liquid crystal q-plate, as shown in the inset of Figure 1 (labeled "Generation of entanglement"). Capitalizing on the optical spin-orbit interaction caused by the metasurface, the quantum state of a single horizontally or vertically polarized photon with zero OAM can be transformed into a Bell state encoded in the dimensions of SAM and OAM. Based on this study, Li et al. proposed a modified geometric phase metasurface to manipulate one of the polarization-entangled photons for generating high-dimensional entanglement.<sup>[49]</sup> As shown in Figure 5c, the metasurface seamlessly combines the functionalities of a q-plate and a polarization grating. The LCP (RCP) photons pass through the metasurface and are converted into RCP (LCP) vortex photons that propagate along the +1st (-1st) diffraction order with a topological charge of  $2q$  ( $-2q$ ). In this way, a two-photon state generated by a bidirectionally pumped SPDC source,  $(|R\rangle|R\rangle + |L\rangle|L\rangle)/\sqrt{2}$ , is transformed into  $(|R\rangle|2q\rangle|a\rangle|L\rangle + |L\rangle|-2q\rangle|b\rangle|R\rangle)/\sqrt{2}$ , a high-dimensional four-qubit state, where  $a$  ( $b$ ) denotes the photon path corresponding to the +1st (-1st) diffraction. This multifunctional metasurface provides a convenient framework to encode quantum information across multiple DOFs of photons, potentially enhancing the capacity and security of quantum communication.

Apart from the distillation and generation, the transformation and distribution of quantum entanglement can also be conducted by meticulously designed metasurfaces. Gao et al. reported a metasurface known as geometrical-scaling-induced (GSI) metasurface, which diffracts the LP incident light into different diffraction orders with different polarization states.<sup>[50]</sup> The GSI metasurface is composed of birefringent resonators, each of which converts LP light into a circularly polarized state and imparts a GSI phase determined by the geometrical features of the resonator. The superposition of all the diffraction fields from each resonator results in the desired combinations of output beams. The polarizations and propagation direction of these beams can be controlled by the enantiomorphism, size, spatial sequence, and the period of resonators in the metasurface supercell. Soon after, the GSI metasurface was introduced into the field of quantum photonics.<sup>[19]</sup> As shown in Figure 5d, the polarization-entangled photon pairs are spatially separated and directed toward two different GSI metasurfaces, MS1 (with  $M$  diffraction orders) and MS2 (with  $N$  diffraction orders). Each

diffraction order is considered as a distinct output channel. The two entangled photons may be respectively diffracted out from any channel of MS1 and MS2, leading to  $M \times N$  channel pairs for the transformation and distribution of quantum entanglement. By elaborately designing the resonators in the unified supercell, the entangled state distributed to each channel pair appears as a Bell state or a superposition of Bell states. Bell states refer to four maximally entangled states of a two-qubit system, denoted as  $|\phi^\pm\rangle = (|0\rangle_A|0\rangle_B \pm |1\rangle_A|1\rangle_B)/\sqrt{2}$  and  $|\psi^\pm\rangle = (|0\rangle_A|1\rangle_B \pm |1\rangle_A|0\rangle_B)/\sqrt{2}$ , where the subscripts  $A$  and  $B$  represent two different qubits. These four orthonormal Bell states form a complete basis to describe a two-qubit system and provide a valuable platform for implementing diverse quantum information technologies. Figure 5e depicts the experimental setup for generating, transforming and distributing, as well as detecting the two-photon entangled states. The original two-photon Bell state  $|\psi^+\rangle = (|HV\rangle + |VH\rangle)/\sqrt{2}$  is produced by bidirectionally pumping a periodically poled SPDC crystal embedded in a Sagnac interferometer.<sup>[51]</sup> Then, the polarization beam splitter (PBS) separates two entangled photons, which are then transformed and distributed by two metasurfaces, respectively. Finally, the entangled states distributed to each output channel pair are measured through quantum state tomography. The  $2 \times 2$  and  $4 \times 4$  entanglement distributors are designed and fabricated to manipulate two entangled photons in the two paths. As a result, under the illumination of the entangled photon pairs in the Bell state  $|\psi^+\rangle$ , the  $2 \times 2$  distributor operates as a Bell state generator, distributing four Bell states to four different channel pairs. Two of the reconstructed density matrices are demonstrated in Figure 5f, both showing high fidelities compared to the ideal entangled states. In order to quantitatively describe the efficiency of entanglement distribution for each channel pair, the authors define it as the ratio of the two-photon coincidence counts of that channel pair to that of the photon pair source. For the  $2 \times 2$  distributor, the efficiencies of each channel pair are measured as 9.95%, 9.93%, 7.11%, and 6.86%, respectively. The overall transmission efficiency of the metasurface is 33.26%. In the case of the  $4 \times 4$  distributor, it is verified that the consequent entangled states of the 16 channel pairs contain four Bell states, 8 superpositions of 2 Bell states, and 4 superpositions of all Bell states. The average efficiency of the 16 channel pairs is measured as 2.22%, and the overall transmission efficiency of the metasurface increases slightly to 35.56%. Based on this scheme, a large number of photon states can be readily distributed to  $M \times N$  users without a mass of conventional bulky optical elements, which could greatly facilitate the miniaturization and integration of quantum networks.

The metasurface-assisted manipulation of quantum states can also be utilized for quantum state measurements. Conventionally, the measurement of an unknown quantum state is achieved through quantum state tomography, which involves sequentially projecting numerous photons prepared in the same quantum state to a set of measurement bases.<sup>[48]</sup> According to statistical photon counting from various projective measurements, one can reconstruct the density matrix of an unknown quantum state. The projections require various combinations of reconfigurable wave plates, PBSs, and even spatial light modulators in cases involving OAM.<sup>[52]</sup> However, the switching between different projections is time-consuming and unstable

due to potential fluctuations and misalignment among these optical elements. The excellent ability of metasurfaces in manipulating photonic quantum states offers new opportunities to improve and simplify the projection elements in a compact and robust manner. In 2018, Wang et al. proposed to accomplish multiple projections of quantum states simultaneously with a single dielectric metasurface.<sup>[20a]</sup> As shown in Figure 5g, the metasurface consists of  $M/2$  interleaved metagratings, each designed to split two orthogonal elliptical polarization states using the principles of geometric phase and propagation phase, resulting in  $M$  diffracted beams from the entire metasurface. The  $N$ -photon polarization quantum state can be projected into  $M$  different measurement bases and then detected by  $M$  polarization-insensitive single-photon click detectors. For the case with  $N=2$  and  $M=6$ , two polarization-entangled photons pass through the metasurface and arrive at arbitrary combinations of the six ports in each time frame. After recording and totalizing all the two-photon coincidence events over a sufficient amount of time frames, all fifteen twofold correlations between the six ports are obtained, which provides full information for reconstructing the input two-photon density matrix with high fidelity. It is worth mentioning that when dealing with multiphoton quantum states, the required number of output ports  $M$  is proportional to the photon number  $N$ , indicating the appealing scalability of this metasurface-based state reconstruction method. Besides, the metasurface can be integrated with single-photon-sensitive electron-multiplying charge-coupled device (CCD) cameras to ascertain spatial correlations, thereby expediting and simplifying the measurement of multiphoton quantum states.

Bell state measurement (BSM) is an essential procedure in various quantum information technologies, such as quantum teleportation, quantum dense coding, and entanglement swapping.<sup>[53]</sup> Normally, the standard setup for measuring the polarization Bell state consists of a 50:50 beam splitter and two PBSs. However, this configuration can only distinguish two out of the four Bell states, that is, 50% discrimination probability. To actualize perfect BSM, Gao et al. proposed substituting two different polarization-multiplexed metasurfaces for the PBSs in the standard configuration, as shown in Figure 5h.<sup>[20b]</sup> The right panel of Figure 5h displays the constituent supercells  $A$  ( $A'$ ) and  $B$  ( $B'$ ) of the designed binary-pixel metasurface  $M1$  ( $M2$ ), which are exploited for different polarization control in two output paths. Each supercell is composed of eight GaN nanopillars with varying widths and lengths, designed to meet the required polarization control functions based on the propagation phase principle. Between the metasurfaces and the single-photon detectors, there are four polarizers to orientationally project the polarization states of the transmitted photons. Based on this metasurface-enhanced configuration, the two-photon coincidence counting signals from both path  $c$  and  $d$  (in Figure 5h) can directly distinguish only the antisymmetric Bell state  $|\psi^-\rangle$ . While the coincidence counting signals are collected from each path of  $c$  and  $d$ , they give two different linear superpositions of the residual symmetric Bell states  $|\psi^+\rangle$ ,  $|\phi^+\rangle$ , and  $|\phi^-\rangle$ , which are associated with the orientations of four polarizers. By rotating the polarizers to specific angles, the coincidence counting statistics of one symmetric Bell state are anticorrelated with those of the rest two symmetric Bell states, which makes the former distinguishable. According to the two preceding linear superposition

relationship, one can measure two of the symmetric Bell states. Thus, single-coincidence counting measurement makes one antisymmetric and two symmetric Bell states discriminated (75% discrimination probability). After implementing coincidence counting measurements twice under different sets of polarizer orientations, the complete measurement of polarization Bell state is achieved. Compared to other methods aimed at increasing the discrimination probability of BSM, such as introducing auxiliary photons<sup>[54]</sup> or hyperentanglement,<sup>[55]</sup> this metasurface-based BSM scheme effectively reduces the number of bulky optical elements and can be performed by simply rotating the polarizers, bringing out great convenience and feasibility.

Metasurfaces with multiplexing capabilities across different DOFs of photons offer a streamlined solution for the measurement and reconstruction of complex quantum states. For example, Figure 5i shows a well-designed multiplexing metasurface intended for the measurement of single-photon OAM quantum states.<sup>[20c]</sup> Conventionally, the measurement of OAM quantum states depends on the apparatuses such as q-plates,<sup>[56]</sup> spiral phase plates,<sup>[57]</sup> and spatial light modulators loaded with computer-calculated holograms to realize the projection of OAM states.<sup>[58]</sup> To achieve a similar OAM projection, the proposed metasurface is designed to multiplex in three DOFs: path, polarization, and OAM. The metasurface made of elliptical nanopillars acts as a binary vortex grating for horizontal polarization and as a sine/cosine vortex grating for vertical polarization. To be specific, the OAM states of incident photons are chosen to be constructed by the qubit basis ( $|+2\rangle$ ,  $|-2\rangle$ ), where  $\pm 2$  denotes the topological charges. As depicted in Figure 5i, the incident photons with  $|-2\rangle$  OAM state are diffracted into Path1 and Path2 by the metasurface. By diversely setting the OAM evolution in Path1 and Path2 and utilizing the polarization multiplexing of the birefringent metasurface, four different OAM projective bases  $|+2\rangle$ ,  $|-2\rangle$ ,  $(|+2\rangle + |-2\rangle)/\sqrt{2}$ , and  $(|+2\rangle + i|-2\rangle)/\sqrt{2}$  are obtained in a single metasurface, allowing for the single-photon OAM state tomography with high fidelity.

## 4. Applications of Quantum Metasurfaces

Metasurfaces have shown considerable promise in the field of classical optics for light detection, facilitating various applications such as optical sensing,<sup>[59]</sup> imaging,<sup>[60]</sup> polarization and OAM detection,<sup>[61]</sup> and spectral measurement.<sup>[62]</sup> Despite these advancements in the classical domain, metasurfaces can also play a surprising role in detecting nonclassical light by virtue of the nonintuitive quantum entanglement or quantum interference, giving rise to a wide range of novel applications, including quantum sensing,<sup>[23]</sup> quantum weak measurement,<sup>[24]</sup> quantum coherent absorption,<sup>[22,63]</sup> and quantum imaging.<sup>[21,64]</sup>

In terms of quantum sensing, Georgi et al. utilized a metasurface-based interferometer (MBI) to quantify the relative phase between the two components of a quantum superposition state.<sup>[23]</sup> The geometrical phase metasurface is specifically engineered to function as a circular polarization splitter. Due to metasurface-induced quantum interference, an initial quantum state  $|\psi\rangle = (\hat{a}_H^\dagger \hat{a}_V^\dagger)|0\rangle$  in the linear polarization basis will be converted to a two-photon NOON state in the circular polarization basis, that is,  $|\psi\rangle = (\hat{a}_H^\dagger \hat{a}_V^\dagger)|0\rangle = -i/2(\hat{a}_L^\dagger \hat{a}_L^\dagger - \hat{a}_R^\dagger \hat{a}_R^\dagger)|0\rangle$ ,

where  $\hat{a}^\dagger$  is the photon creation operator. Thus, when a single-photon pair (with the initial quantum state of  $|\psi\rangle = (\hat{a}_H^\dagger \hat{a}_V^\dagger)|0\rangle$ ) from SPDC source interacts with the proposed metasurface, the two photons bunch within either of the two output ports of the metasurface, resulting in path entanglement. In contrast, when the photon pair passes through the metasurface for a second time, the path-entangled two-photon state becomes spatially disentangled as its state is restored back to  $|\psi\rangle = (\hat{a}_H^\dagger \hat{a}_V^\dagger)|0\rangle$ . **Figure 6a** presents a schematic representation of the constructed MBI, in which the photon pair passes through the metasurface twice. A tilted 130  $\mu\text{m}$ -thick glass plate is inserted in the upper arm of the interferometer to change the phase delay  $\varphi$  between the two optical paths. Accordingly, the output state can be derived as  $|\psi\rangle_\varphi = -i/2(\hat{a}_L^\dagger \hat{a}_L^\dagger e^{-i2\varphi} - \hat{a}_R^\dagger \hat{a}_R^\dagger)|0\rangle = 1/2(e^{-i2\varphi} + 1)\hat{a}_H^\dagger \hat{a}_V^\dagger|0\rangle - i/4(e^{-i2\varphi} - 1)(\hat{a}_H^\dagger \hat{a}_H^\dagger - \hat{a}_V^\dagger \hat{a}_V^\dagger)|0\rangle$ . It's obvious that the output state will remain identical to the initial state  $\hat{a}_H^\dagger \hat{a}_V^\dagger|0\rangle$  for  $\varphi = n\pi$  ( $n \in \mathbb{Z}$ ), whereas it will be  $1/2(\hat{a}_H^\dagger \hat{a}_H^\dagger - \hat{a}_V^\dagger \hat{a}_V^\dagger)|0\rangle$  for  $\varphi = (n + 1/2)\pi$  ( $n \in \mathbb{Z}$ ). In the former case, the two output photons are separated by the PBS, with one photon detected by detector A and the rest one collected by detector B, leading to the maximum coincidence rate between the two detectors. In the latter case, two photons bunch at either the detector A or detector B, resulting in the minimum coincidence rate. More generally, the coincidence rate is theoretically and experimentally demonstrated to oscillate with the phase

delay  $\varphi$ , following a  $\cos^2(\varphi)$  function. The findings confirm that the metasurface can not only retain quantum coherence (i.e., the phase information in the quantum superposition state) but also provides a viable strategy for quantum sensing and measurement utilizing the phase sensitivity of the coincidence rate.

Metasurfaces can also contribute to an essential aspect of quantum detection, namely, weak measurements.<sup>[24]</sup> The upper panel of Figure 6b illustrates the concept of weak measurement, which was initially developed in electronic system as an improvement over Stern–Gerlach experiment. In this experiment, the original magnetic field is intentionally set to be extremely weak to interact with the preselected electron spin quantum state, and an additional strong magnetic field in a perpendicular direction is introduced to postselect the final state. It is crucial to ensure that the preselected quantum state remains nearly undisturbed when coupled with the weak magnetic field. The amplification effect resulting from the postselection process enables the acquisition of a significant observable physical quantity (in this case, the transverse distribution of the electron beam) that reflects the quantum information of the measured state. In the context of weak measurement in optics, the initial state refers to the polarization state of the incident photons, which is preselected by the first Glan laser polarizer (GLP1). A tiny phase gradient created by a dielectric metasurface acts like the weak magnetic field in an electronic system, which endows the spin photons slight momentum shifts. A quarter-wave plate and GLP2 are then used to postselect different final states. By rotating the quarter-wave

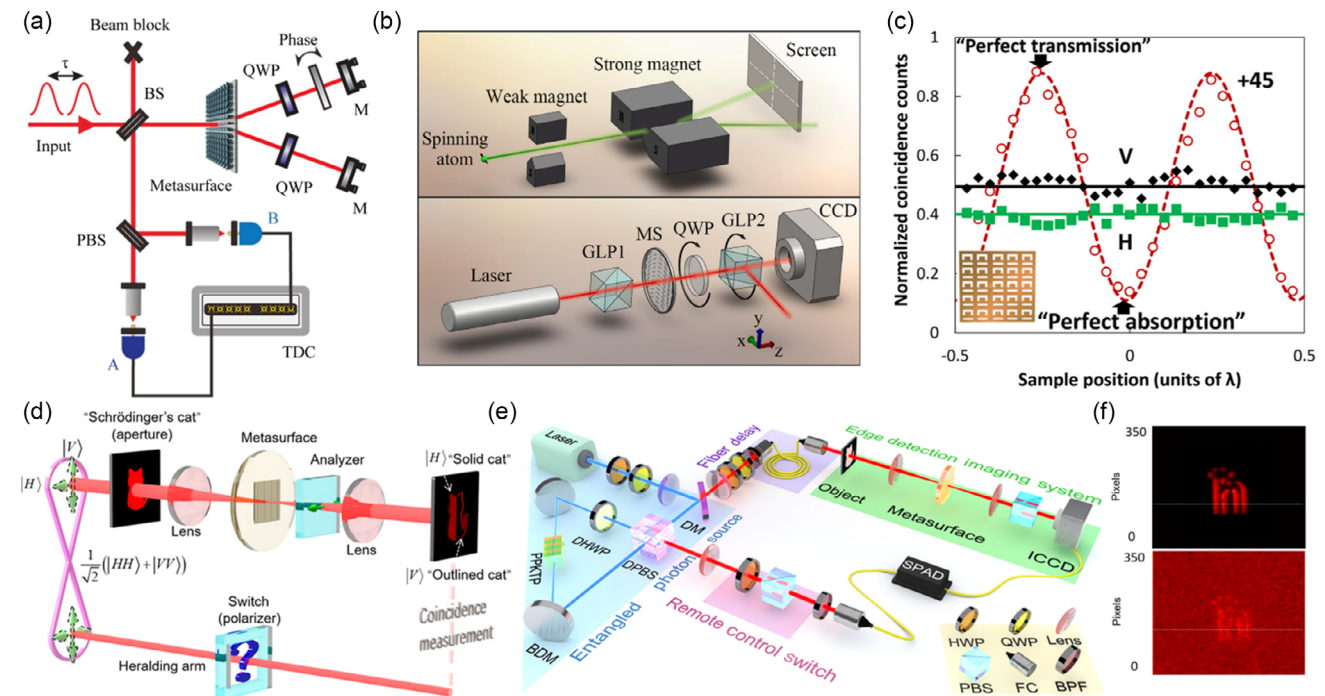


**Figure 6.** Diversified applications of quantum metasurfaces. a) MBI for detecting the phase information in a quantum superposition state. Reproduced under terms of the CC-BY license.<sup>[23]</sup> Copyright 2019, The Authors, published by Springer Nature. b) Comparison of quantum weak measurements in an electronic system and a metasurface-based optical system. Reproduced with permission.<sup>[24]</sup> Copyright 2017, AIP Publishing. c) Coherent perfect absorption of entangled photons in a plasmonic metasurface. Reproduced with permission.<sup>[63a]</sup> Copyright 2017, ACS. d) Switchable quantum edge detection supported by a geometric phase metasurface. e) Experimental setup for implementing quantum edge detection. f) Edge detection images obtained from coincidence imaging (upper) and direct imaging (lower). (d–f) Reproduced under terms of the CC-BY license.<sup>[21]</sup> Copyright 2020, The Authors, published by AAAS.

plate and GLP2, the tiny shifts in the position and momentum of the photon wavefunction are amplified and observed in the beam intensity distribution collected by the CCD. The presented metasurface-based weak measurement, implemented with a simple setup and easy operability, offers an effective method for analyzing the wavefunction of photon quantum states.

The metasurface-enabled coherent absorption was initially demonstrated by Zhang et al, showcasing a 100% light-by-light modulation without the use of nonlinear media.<sup>[65]</sup> In order to attain a modulation efficiency of 100%, a plasmonic metasurface is engineered to absorb 50% of incident light when illuminated by a traveling wave. Next, the well-designed metasurface is placed in a Sagnac-style interferometer. Due to the interference of two counterpropagating coherent light beams, the metasurface can exhibit complete light absorption or transparency, depending on the relative phase between the beams. This process not only introduces an innovative method for surpassing the theoretical constraint of 50% absorption in ultrathin films,<sup>[66]</sup> but also inspires the development of high-performance solar cells, optical filters, and modulators. It's worth noting that this coherent perfect absorption process is independent of the intensity of light and can operate even with extremely low power levels. Roger et al. demonstrated that coherent perfect absorption can also be observed in the single-photon regime.<sup>[22]</sup> In their experimental setup, the photon pair generated from a SPDC crystal is separated, with one photon being launched into the interferometer and the other photon used for heralding. It's founded that the signal photon in the interferometer can be deterministically absorbed or transmitted by translating the metasurface along the beam propagation direction, as a standing wave is formed through single-photon interference. However, when one of the input channels of the metasurface is blocked, the interference ceases to exist, and the single photon from the traveling wave will be absorbed with a 50% probability. Moreover, Altuzarra et al. successfully confirmed the quantum nonlocal correlation of two polarization-entangled photons by adapting the interferometer to be polarization sensitive.<sup>[63a]</sup> The modification involves two steps. First, a polarizer is added to the idler photon channel to select the idler photon's polarization and project the signal photon into the corresponding polarization. Second, a half-wave plate is introduced into one of the arms of the interferometer to manipulate the path-entangled state of the signal photon. By rotating the polarizer, the path distinguishability of the signal photon is either created or erased, which determines whether a standing wave can be formed at the metasurface. As shown in Figure 6c, the absorption of signal photons can be remotely controlled by selectively detecting the polarization of idler photons. If the idler photon is selected to be horizontally or vertically polarized, the absorption of the signal photon is probabilistic and approximates the traveling wave absorption of the metasurface. Instead, when the idler photon is selected to be LP at 45°, the path distinguishability of the signal photon is erased, leading to the formation of a standing wave and the deterministic dependence of signal photon absorption on the metasurface position. A recent study conducted by Lyons et al. demonstrated that the coherent absorption enabled by a lossy metasurface can also be applied to multiphoton states.<sup>[63b]</sup> In their experiment, both photons of a photon pair were injected into the interferometer, and the metasurface exhibited

a two-photon absorption of 40%, which approaches the theoretical maximum and is twice that of a classical absorption process. The quantum coherent absorption process provides a new opportunity to investigate the mechanism of quantum interference and to potentially realize quantum logic gates by precisely controlling the absorption of quantum light.

Recently, metasurfaces have emerged as a promising tool for quantum imaging employing nonclassical photon-pair sources.<sup>[21,64,67]</sup> In these imaging systems, only the signal photons, which are heralded by the idler photons, interact with the metasurface and participate in the imaging process. Compared to imaging with classical light, the nonlocal correlation of photon pairs holds a distinct advantage: the imaging operation in the signal arm can be remotely controlled by the heralding arm without any adjustments in the signal arm. For example, Altuzarra et al. imprinted two overlapping polarizing patterns on a metasurface: a star and a triangle. These patterns acted as polarizers, allowing only horizontally and vertically polarized light to transmit, respectively.<sup>[64a]</sup> When the signal photons from polarization-entangled photon pairs irradiate the metasurface, the resulting image can be deterministically switched between the star and the triangle by selectively measuring the polarization of idler photons. However, in the case of unentangled input photons, a superimposed image of both patterns is obtained. Based on this heralded single-photon imaging technique, Zhou et al. proposed an advanced version of remote quantum imaging control.<sup>[21]</sup> As shown in Figure 6d, a geometric metasurface placed in a 4f system is used to induce the photonic spin Hall effect to achieve edge detection. The input two-photon polarization-entangled state of this switchable edge detection system is selected as  $(|HH\rangle + |VV\rangle)/\sqrt{2}$ . After the beam of signal photons with unknown linear polarization passes through the cat-shaped aperture, it will be separated by the metasurface into LCP and RCP components with a lateral shift. In the region where LCP and RCP components overlap, the beam's polarization will be recovered to the same linear polarization as that of the signal photons. In the nonoverlapping region, the beam maintains circular polarization, and its shape precisely matches the outline of the cat. Utilizing quantum entanglement to nonlocally determine the polarization of signal photons, the LP output beam in the overlapping region can be selectively blocked or transmitted through a linear polarizer, which enables the activation or deactivation of edge detection. Figure 6e shows the experimental setup for implementing quantum edge detection. Once an idler photon is detected by a single-photon avalanche detector (SPAD), an electrical signal is sent to the intensified charge-coupled device (ICCD) camera, triggering the camera to be exposed in an ultrashort time window to capture the corresponding signal photon. So, the noise is only accumulated within the ultrashort coincidence time window, resulting in a superior signal-to-noise ratio (SNR) of the edge image compared to the direct imaging where the camera is continuously exposed. The improvement of the SNR in edge images is evident from Figure 6f, where the upper edge image is obtained through coincidence imaging and the lower one through direct imaging. Similarly, Yang et al. demonstrated quantum vectorial holography by illuminating the heralded signal photons onto a multichannel polarization-multiplexed metasurface.<sup>[64b]</sup> By choosing different input and output polarization channels, three distinct holographic images

as well as their combinations can be reconstructed, showcasing the high information density of the proposed quantum imaging system. The incorporation of functional metasurfaces into the heralded the single-photon imaging technique shows great potential for developing novel imaging and image processing schemes with appealing SNR and reliability.

## 5. Conclusion and Outlook

In this article, we present an overview of the recent significant advancements in the rapidly evolving field of quantum metasurfaces. First, we focus on two kinds of quantum light sources based on metasurfaces, the SPEs, and SPDC photon-pair sources. The integration of SPEs and metasurfaces can be realized in two configurations, wherein the metasurfaces function as metalenses or photon-plasmon-photon converters to improve the collection efficiency and engineer the single-photon emission in multiple DOFs. As for the SPDC photon-pair sources, metasurfaces typically support various resonances to increase the density of states and facilitate the SPDC process in nonlinear crystals. Specifically, metasurfaces can be used to generate an AQV in the far field, which provides a practical and realistic strategy to regulate the radiation characteristics of multilevel atomic QEs. Then, we review the manipulation and measurement of quantum states with the assistance of metasurfaces. The compact and efficient generation, distillation, transformation, and distribution of entangled states are successively demonstrated by leveraging the design flexibility and versatility offered by metasurfaces. The lossless dielectric metasurfaces can be used to replace the conventional bulky projection elements, enabling the construction of compact and robust quantum state tomography systems for high-fidelity reconstruction of quantum states. Finally, we summarize several exemplary applications of metasurfaces in nonclassical light detection, including quantum sensing, quantum weak measurement, coherent perfect absorption of quantum light, and quantum imaging.

Due to the sophisticated nanostructures of metasurfaces, their manipulation of quantum light is inevitably constrained by fabrication errors. The fabrication errors of metasurfaces typically stem from under-etching or over-etching processes, which can cause the actual lateral dimensions of all meta-atoms to be larger or smaller than the designed values, while maintaining the periodicities of the meta-atoms close to the design values. These errors can deviate metasurfaces from their intended functions, such as disrupting the frequency, direction, polarization, and mode purity of the output beam of a quantum light source, reducing the fidelity of quantum state control and measurement, among other consequences. There are several approaches available to address this concern. One strategy is to optimize the fabrication procedure of metasurfaces to improve fabrication accuracy. Another alternative is to utilize geometric phase metasurfaces in place of resonant phase and propagation phase metasurfaces. Unlike the latter two types of metasurfaces, where the size of the meta-atoms is a critical factor, geometric phase metasurfaces achieve phase control by rotating the orientation of the meta-atoms, exhibiting strong robustness to errors in meta-atom size. For certain applications of metasurfaces, such as quantum state measurement and reconstruction, it is common practice to

characterize the fabricated metasurface using classical light before quantum measurement, in order to determine the transfer matrix that includes all the fabrication imperfections of the metasurface.<sup>[20a]</sup> Using the transfer matrix, precise corrections can be made to quantum measurement outcomes, effectively reducing the impact of fabrication errors on the results of quantum measurements.

Despite all the remarkable advances signifying that metasurfaces have introduced a new paradigm for exploring quantum phenomena by simultaneously controlling multiple DOFs of photons, the full potential of metasurfaces in quantum optics remains unachieved. Further investigation is necessary to overcome existing challenges. For example, although the theoretical proposal of far-field AQV-induced quantum interference between two orthogonal transitions of atomic QEs facilitated by metasurfaces exists, the corresponding experimental setup has not been achieved yet. In addition, a challenge in metasurface-based photon-pair sources is how to directly produce photon pairs with desired quantum states encoded in different DOFs, similar to the cases of single-photon sources. Ma et al. made an instructive attempt by improving their metasurface design in Figure 3d. By leveraging the principle that the polarization of emitted photon pairs aligns with the metagrating's orientation, it is theoretically feasible to achieve arbitrary two-photon polarization-entangled qutrit states by integrating three distinctively oriented metagratings into a unified metasurface.<sup>[68]</sup> Apart from this scheme, we anticipate a growing number of innovative metasurface-based photon-pair sources capable of generating diverse entangled states.

On the other hand, the vast majority of metasurfaces that has been used in manipulating quantum states lack real-time tunability or reconfigurability. Metasurfaces composed of static structures often feature fixed optical functionalities, rendering them unsuitable for addressing the intricate and variable requirements of quantum information processing. An effective approach is to integrate or fabricate metasurfaces with tunable optical materials such as graphene, semiconductors, liquid crystals, nonlinear materials, and phase-change materials, among others.<sup>[69]</sup> By subjecting the metasurfaces to mechanical stress or applying external electrical, optical, and thermal fields, it becomes feasible to dynamically manipulate quantum states. Impressively, Kort-Kamp et al. presented the concept of space-time quantum metasurfaces (STQMs) for continuously molding quantum light in both space and time domains.<sup>[70]</sup> When passing through the STQM, the input single-photon state will evolve into a state with color-spin-path hyperentanglement, showcasing the powerful ability of STQMs in manipulating quantum states across multiple DOFs. The development of dynamical STQMs shows promising potential for catalyzing breakthroughs in quantum optics and stimulating the emergence of novel photonic devices, including nonreciprocal quantum routers and active quantum sensors.

Furthermore, investigating innovative approaches that go beyond the traditional design principles of classical metasurfaces to create advanced quantum metasurfaces represents an intriguing area for further research. For instance, Bozhevolnyi et al. recently proposed an enlightening method called scattering holography to design quantum emitter-coupled metasurfaces capable of generating single-photon emissions with predesigned

sizes, polarizations, and propagation directions.<sup>[71]</sup> Unlike the previous cases illustrated in Figure 2d–e, they adopt the QE-excited radially diverging SPPs as reference waves, while designating the in-plane electric field components of desired single-photon emissions as signal waves. The holographic metasurface is constructed based on the interference pattern created by reference and signal waves. The invention of novel design schemes like this will inject new vitality into the development of quantum metasurfaces. For readers seeking further insights into the future development of quantum metasurfaces, it is advisable to refer to additional pertinent reviews published recently.<sup>[72]</sup> Based on the above discussion, it is conceivable that the convergence of metasurfaces and quantum photonics will greatly expedite the discovery of new quantum physics and facilitate the on-chip integration of quantum information systems.

## Acknowledgements

This work was supported by the National Key Research and Development Program of China (2021YFA1400601 and 2022YFA1404501), the National Natural Science Fund for Distinguished Young Scholar (11925403), and the National Natural Science Foundation of China (12122406 and 12192253).

## Conflict of Interest

The authors declare no conflict of interest.

## Keywords

metasurfaces, quantum entanglement and interference, quantum information, quantum photonics

Received: December 30, 2023

Revised: March 20, 2024

Published online:

- [1] J. L. O'Brien, *Science* **2007**, *318*, 1567.  
 [2] R. Hanson, L. P. Kouwenhoven, J. R. Petta, S. Tarucha, L. M. K. Vandersypen, *Rev. Mod. Phys.* **2007**, *79*, 1217.  
 [3] E. Urban, T. A. Johnson, T. Henage, L. Isenhower, D. D. Yavuz, T. G. Walker, M. Saffman, *Nat. Phys.* **2009**, *5*, 110.  
 [4] L. M. K. Vandersypen, M. Steffen, G. Breyta, C. S. Yannoni, M. H. Sherwood, I. L. Chuang, *Nature* **2001**, *414*, 883.  
 [5] M. H. Devoret, R. J. Schoelkopf, *Science* **2013**, *339*, 1169.  
 [6] N. Yu, P. Genevet, M. A. Kats, F. Aieta, J. P. Tetienne, F. Capasso, Z. Gaburro, *Science* **2011**, *334*, 333.  
 [7] W. Liu, Z. Li, M. A. Ansari, H. Cheng, J. Tian, X. Chen, S. Chen, *Adv. Mater.* **2023**, *35*, 2208884.  
 [8] C. Pfeiffer, N. K. Emani, A. M. Shaltout, A. Boltasseva, V. M. Shalaev, A. Grbic, *Nano Lett.* **2014**, *14*, 2491.  
 [9] F. Aieta, M. A. Kats, P. Genevet, F. Capasso, *Science* **2015**, *347*, 1342.  
 [10] Z. Liu, Z. Li, Z. Liu, J. Li, H. Cheng, P. Yu, W. Liu, C. Tang, C. Gu, J. Li, S. Chen, J. Tian, *Adv. Funct. Mater.* **2015**, *25*, 5428.  
 [11] a) Y. Zhao, A. Alù, *Nano Lett.* **2013**, *13*, 1086; b) M. Khorasaninejad, F. Capasso, *Science* **2017**, *358*, eaam8100; c) A. Pors, M. G. Nielsen, S. I. Bozhevolnyi, *Optica* **2015**, *2*, 716; d) G. Zheng, H. Mühlenbernd, M. Kenney, G. Li, T. Zentgraf, S. Zhang, *Nat. Nanotechnol.* **2015**, *10*, 308; e) W. Ye, F. Zeuner, X. Li, B. Reineke, S. He, C. W. Qiu, J. Liu, Y. Wang, S. Zhang, T. Zentgraf, *Nat. Commun.* **2016**, *7*, 11930;  
 f) S. Chen, Y. Cai, G. Li, S. Zhang, K. W. Cheah, *Laser Photonics Rev.* **2016**, *10*, 322.  
 [12] S. Jia, Y. Li, Z. Xue, K. Chen, Z. Li, Q. Gong, J. Chen, *Adv. Mater.* **2023**, *35*, 2212244.  
 [13] N. V. Proscia, Z. Shotan, H. Jayakumar, P. Reddy, C. Cohen, M. Dollar, A. Alkauskas, M. Doherty, C. A. Meriles, V. M. Menon, *Optica* **2018**, *5*, 1128.  
 [14] Y. Kan, F. Ding, C. Zhao, S. I. Bozhevolnyi, *ACS Photonics* **2020**, *7*, 1111.  
 [15] a) L. Li, Z. Liu, X. Ren, S. Wang, V. C. Su, M. K. Chen, C. H. Chu, H. Y. Kuo, B. Liu, W. Zang, G. Guo, L. Zhang, Z. Wang, S. Zhu, D. P. Tsai, *Science* **2020**, *368*, 1487; b) J. Zhang, J. Ma, M. Parry, M. Cai, R. Camacho-Morales, L. Xu, D. N. Neshev, A. A. Sukhorukov, *Sci. Adv.* **2022**, *8*, eabq4240.  
 [16] a) T. Santiago-Cruz, A. Fedotova, V. Sultanov, M. A. Weissflog, D. Arslan, M. Younesi, T. Pertsch, I. Staude, F. Setzpfandt, M. Chekhova, *Nano Lett.* **2021**, *21*, 4423; b) C. Son, V. Sultanov, T. Santiago-Cruz, A. P. Anthur, H. Z. Zhang, R. Paniagua-Dominguez, L. Krivitsky, A. I. Kuznetsov, M. V. Chekhova, *Nanoscale* **2023**, *15*, 2567; c) T. Santiago-Cruz, S. D. Gennaro, O. Mitrofanov, S. Addamane, J. Reno, I. Brener, M. V. Chekhova, *Science* **2022**, *377*, 991.  
 [17] a) M. Asano, M. Bechu, M. Tame, Ş. Kaya Özdemir, R. Ikuta, D. Ö. Güney, T. Yamamoto, L. Yang, M. Wegener, N. Imoto, *Sci. Rep.* **2015**, *5*, 18313; b) D. Zhang, Y. Chen, S. C. Gong, W. Wu, W. Cai, M. X. Ren, X. F. Ren, S. Zhang, G. C. Guo, J. J. Xu, *Light Sci. Appl.* **2022**, *11*, 58.  
 [18] T. Stav, A. Faerman, E. Maguid, D. Oren, V. Kleiner, E. Hasman, M. Segev, *Science* **2018**, *361*, 1101.  
 [19] Y. J. Gao, Z. Wang, Y. Jiang, R. W. Peng, Z. Y. Wang, D. X. Qi, R. H. Fan, W. J. Tang, M. Wang, *Phys. Rev. Lett.* **2022**, *129*, 023601.  
 [20] a) K. Wang, J. G. Titchener, S. S. Kruk, L. Xu, H. P. Chung, M. Parry, I. I. Kravchenko, Y. H. Chen, A. S. Solntsev, Y. S. Kivshar, D. N. Neshev, A. A. Sukhorukov, *Science* **2018**, *361*, 1104; b) Z. Gao, Z. Su, Q. Song, P. Genevet, K. E. Dorfman, *Nanophotonics* **2023**, *12*, 569; c) M. Wang, L. Chen, D. Y. Choi, S. Huang, Q. Wang, C. Tu, H. Cheng, J. Tian, Y. Li, S. Chen, H. T. Wang, *Nano Lett.* **2023**, *23*, 3921.  
 [21] J. Zhou, S. Liu, H. Qian, Y. Li, H. Luo, S. Wen, Z. Zhou, G. Guo, B. Shi, Z. Liu, *Sci. Adv.* **2020**, *6*, eabc4385.  
 [22] T. Roger, S. Vezzoli, E. Bolduc, J. Valente, J. J. F. Heitz, J. Jeffers, C. Soci, J. Leach, C. Couteau, N. I. Zheludev, D. Faccio, *Nat. Commun.* **2015**, *6*, 7031.  
 [23] P. Georgi, M. Massaro, K. H. Luo, B. Sain, N. Montaut, H. Herrmann, T. Weiss, G. Li, C. Silberhorn, T. Zentgraf, *Light Sci. Appl.* **2019**, *8*, 70.  
 [24] S. Z. Chen, X. X. Zhou, C. Q. Mi, Z. X. Liu, H. L. Luo, S. C. Wen, *Appl. Phys. Lett.* **2017**, *110*, 161115.  
 [25] M. Hijlkema, B. Weber, H. P. Specht, S. C. Webster, A. Kuhn, G. Remppe, *Nat. Phys.* **2007**, *3*, 253.  
 [26] T. Basché, W. E. Moerner, M. Orrit, H. Talon, *Phys. Rev. Lett.* **1992**, *69*, 1516.  
 [27] Y. Bao, Q. Lin, R. Su, Z. K. Zhou, J. Song, J. Li, X. H. Wang, *Sci. Adv.* **2020**, *6*, eaba8761.  
 [28] C. Palacios-Berraquero, D. M. Kara, A. R. P. Montblanch, M. Barbone, P. Latawiec, D. Yoon, A. K. Ott, M. Loncar, A. C. Ferrari, M. Atature, *Nat. Commun.* **2017**, *8*, 15093.  
 [29] C. Wu, S. Kumar, Y. Kan, D. Komisar, Z. Wang, S. I. Bozhevolnyi, F. Ding, *Sci. Adv.* **2022**, *8*, eabk3075.  
 [30] Y. M. He, G. Clark, J. R. Schaibley, Y. He, M. C. Chen, Y. J. Wei, X. Ding, Q. Zhang, W. Yao, X. Xu, C. Y. Lu, J. W. Pan, *Nat. Nanotechnol.* **2015**, *10*, 497.  
 [31] P. Senellart, G. Solomon, A. White, *Nat. Nanotechnol.* **2017**, *12*, 1026.

- [32] A. Vaskin, R. Kolkowski, A. F. Koenderink, I. Staude, *Nanophotonics* **2019**, *8*, 1151.
- [33] T. Y. Huang, R. R. Grote, S. A. Mann, D. A. Hopper, A. L. Exarhos, G. G. Lopez, A. R. Klein, E. C. Garnett, L. C. Bassett, *Nat. Commun.* **2019**, *10*, 2392.
- [34] C. Li, J. Jang, T. Badloe, T. Yang, J. Kim, J. Kim, M. Nguyen, S. A. Maier, J. Rho, H. Ren, I. Aharonovich, *eLight* **2023**, *3*, 19.
- [35] S. Liu, A. Vaskin, S. Addamane, B. Leung, M. C. Tsai, Y. Yang, P. P. Vabishchevich, G. A. Keeler, G. Wang, X. He, Y. Kim, N. F. Hartmann, H. Htoon, S. K. Doorn, M. Zilk, T. Pertsch, G. Balakrishnan, M. B. Sinclair, I. Staude, I. Brener, *Nano Lett.* **2018**, *18*, 6906.
- [36] T. Santiago-Cruz, V. Sultanov, H. Zhang, L. A. Krivitsky, M. V. Chekhova, *Opt. Lett.* **2021**, *46*, 653.
- [37] C. Okoth, A. Cavanna, T. Santiago-Cruz, M. V. Chekhova, *Phys. Rev. Lett.* **2019**, *123*, 263602.
- [38] K. P. Heeg, H. C. Wille, K. Schlage, T. Guryeva, D. Schumacher, I. Uschmann, K. S. Schulze, B. Marx, T. Kämpfer, G. G. Paulus, R. Röhlberger, J. Evers, *Phys. Rev. Lett.* **2013**, *111*, 073601.
- [39] G. X. Li, F. L. Li, S. Y. Zhu, *Phys. Rev. A* **2001**, *64*, 013819.
- [40] a) V. Yannopoulos, E. Paspalakis, N. V. Vitanov, *Phys. Rev. Lett.* **2009**, *103*, 063602; b) Y. Gu, L. Wang, P. Ren, J. Zhang, T. Zhang, O. J. F. Martin, Q. Gong, *Nano Lett.* **2012**, *12*, 2488.
- [41] P. K. Jha, X. Ni, C. Wu, Y. Wang, X. Zhang, *Phys. Rev. Lett.* **2015**, *115*, 025501.
- [42] P. K. Jha, N. Shitrit, X. Ren, Y. Wang, X. Zhang, *Phys. Rev. Lett.* **2018**, *121*, 116102.
- [43] H. Yu, X. Cui, X. Xu, W. Yao, *Natl. Sci. Rev.* **2015**, *2*, 57.
- [44] K. F. Mak, K. He, J. Shan, T. F. Heinz, *Nat. Nanotechnol.* **2012**, *7*, 494.
- [45] a) A. M. Jones, H. Yu, N. J. Ghimire, S. Wu, G. Aivazian, J. S. Ross, B. Zhao, J. Yan, D. G. Mandrus, D. Xiao, W. Yao, X. Xu, *Nat. Nanotechnol.* **2013**, *8*, 634; b) G. Wang, X. Marie, B. L. Liu, T. Amand, C. Robert, F. Cadiz, P. Renucci, B. Urbaszek, *Phys. Rev. Lett.* **2016**, *117*, 187401.
- [46] E. Altevischer, M. P. van Exter, J. P. Woerdman, *Nature* **2002**, *418*, 304.
- [47] S. A. Uriri, T. Tashima, X. Zhang, M. Asano, M. Bechu, D. Ö. Güney, T. Yamamoto, Ş. K. Özdemir, M. Wegener, M. S. Tame, *Phys. Rev. A* **2018**, *97*, 053810.
- [48] D. F. V. James, P. G. Kwiat, W. J. Munro, A. G. White, *Phys. Rev. A* **2001**, *64*, 052312.
- [49] Z. X. Li, D. Zhu, P. C. Lin, P. C. Huo, H. K. Xia, M. Z. Liu, Y. P. Ruan, J. S. Tang, M. Cai, H. D. Wu, C. Y. Meng, H. Zhang, P. Chen, T. Xu, K. Y. Xia, L. J. Zhang, Y. Q. Lu, *Photon. Res.* **2022**, *10*, 2702.
- [50] Y. J. Gao, X. Xiong, Z. Wang, F. Chen, R. W. Peng, M. Wang, *Phys. Rev. X* **2020**, *10*, 031035.
- [51] T. Kim, M. Fiorentino, F. N. C. Wong, *Phys. Rev. A* **2006**, *73*, 012316.
- [52] B. Jack, J. Leach, H. Ritsch, S. M. Barnett, M. J. Padgett, S. Franke-Arnold, *New J. Phys.* **2009**, *11*, 103024.
- [53] D. Bouwmeester, H. Weinfurter, A. Zeilinger, N. Gisin, J. G. Rarity, G. Weihs, J. W. Pan, S. Bose, V. Vedral, P. L. Knight, in *The Physics of Quantum Information: Quantum Cryptography, Quantum Teleportation, Quantum Computation* (Eds: D. Bouwmeester, A. Ekert, A. Zeilinger), Springer, Berlin, Heidelberg **2000**.
- [54] a) S. Wein, K. Heshami, C. A. Fuchs, H. Krovi, Z. Dutton, W. Tittel, C. Simon, *Phys. Rev. A* **2016**, *94*, 032332; b) W. P. Grice, *Phys. Rev. A* **2011**, *84*, 042331.
- [55] a) X. M. Jin, J. G. Ren, B. Yang, Z. H. Yi, F. Zhou, X. F. Xu, S. K. Wang, D. Yang, Y. F. Hu, S. Jiang, T. Yang, H. Yin, K. Chen, C. Z. Peng, J. W. Pan, *Nat. Photonics* **2010**, *4*, 376; b) H. Zhang, C. Zhang, X. M. Hu, B. H. Liu, Y. F. Huang, C. F. Li, G. C. Guo, *Phys. Rev. A* **2019**, *99*, 052301.
- [56] L. J. Kong, R. Liu, W. R. Qi, Z. X. Wang, S. Y. Huang, Q. Wang, C. Tu, Y. Li, H. T. Wang, *Sci. Adv.* **2019**, *5*, eaat9206.
- [57] J. Kysela, M. Erhard, A. Hochrainer, M. Krenn, A. Zeilinger, *Proc. Natl. Acad. Sci. USA* **2020**, *117*, 26118.
- [58] a) Y. Li, S. Y. Huang, M. Wang, C. Tu, X. L. Wang, Y. Li, H. T. Wang, *Phys. Rev. Lett.* **2023**, *130*, 050805; b) B. Y. Wei, W. Hu, Y. Ming, F. Xu, S. Rubin, J. G. Wang, V. Chigrinov, Y. Q. Lu, *Adv. Mater.* **2014**, *26*, 1590.
- [59] a) N. L. Kazanskiy, S. N. Khonina, M. A. Butt, *Nanomaterials* **2023**, *13*, 118; b) J. Qin, S. Jiang, Z. Wang, X. Cheng, B. Li, Y. Shi, D. P. Tsai, A. Q. Liu, W. Huang, W. Zhu, *ACS Nano* **2022**, *16*, 11598.
- [60] M. Pan, Y. Fu, M. Zheng, H. Chen, Y. Zang, H. Duan, Q. Li, M. Qiu, Y. Hu, *Light Sci. Appl.* **2022**, *11*, 195.
- [61] a) B. Yang, D. Ma, W. Liu, D. Y. Choi, Z. Li, H. Cheng, J. Tian, S. Chen, *Optica* **2022**, *9*, 217; b) Y. Guo, S. Zhang, M. Pu, Q. He, J. Jin, M. Xu, Y. Zhang, P. Gao, X. Luo, *Light Sci. Appl.* **2021**, *10*, 63.
- [62] a) M. Faraji-Dana, E. Arbabi, A. Arbabi, S. M. Kamali, H. Kwon, A. Faraon, *Nat. Commun.* **2018**, *9*, 4196; b) R. Wang, M. A. Ansari, H. Ahmed, Y. Li, W. Cai, Y. Liu, S. Li, J. Liu, L. Li, X. Chen, *Light Sci. Appl.* **2023**, *12*, 103.
- [63] a) C. Altuzarra, S. Vezzoli, J. Valente, W. Gao, C. Soci, D. Faccio, C. Couteau, *ACS Photonics* **2017**, *4*, 2124; b) A. Lyons, D. Oren, T. Roger, V. Savinov, J. Valente, S. Vezzoli, N. I. Zheludev, M. Segev, D. Faccio, *Phys. Rev. A* **2019**, *99*, 011801.
- [64] a) C. Altuzarra, A. Lyons, G. Yuan, C. Simpson, T. Roger, J. S. Ben-Jamin, D. Faccio, *Phys. Rev. A* **2019**, *99*, 020101; b) J. Z. Yang, R. Z. Zhao, Z. Meng, J. Li, Q. Y. Wu, L. L. Huang, A. N. Zhang, *Photon. Res.* **2022**, *10*, 2607.
- [65] J. Zhang, K. F. MacDonald, N. I. Zheludev, *Light Sci. Appl.* **2012**, *1*, e18.
- [66] C. Hägglund, S. P. Apell, B. Kasemo, *Nano Lett.* **2010**, *10*, 3135.
- [67] J. Liu, X. Zhu, Y. Zhou, X. Zou, Z. Qin, S. Wang, S. Zhu, Z. Wang, *Opt. Express* **2023**, *31*, 6217.
- [68] J. Ma, J. Zhang, Y. Jiang, T. Fan, M. Parry, D. N. Neshev, A. A. Sukhorukov, *Nano Lett.* **2023**, *23*, 8091.
- [69] T. Cui, B. Bai, H. B. Sun, *Adv. Funct. Mater.* **2019**, *29*, 1806692.
- [70] W. J. M. Kort-Kamp, A. K. Azad, D. A. R. Dalvit, *Phys. Rev. Lett.* **2021**, *127*, 043603.
- [71] a) D. Komisar, S. Kumar, Y. Kan, C. Meng, L. F. Kulikova, V. A. Davydov, V. N. Agafonov, S. I. Bozhevolnyi, *Nat. Commun.* **2023**, *14*, 6253; b) Y. Kan, S. I. Bozhevolnyi, *Adv. Opt. Mater.* **2022**, *10*, 2102697.
- [72] a) K. Wang, M. Chekhova, Y. Kivshar, *Phys. Today* **2022**, *75*, 38; b) F. Ding, S. I. Bozhevolnyi, *Mater. Today* **2023**, *71*, 63.



**Yangwu Li** is a Ph.D. student at the School of Physics, Nankai University, China. He received his B.S. in optoelectronic information science and engineering in 2019 and his M.S. in optical engineering in 2022 from Northwestern Polytechnical University. His current research focuses on the application of metasurfaces in quantum optics.



**Shuqi Chen** is a professor at the Key Laboratory of Weak Light Nonlinear Photonics, Ministry of Education, School of Physics and TEDA Institute of Applied Physics, Nankai University, China. He received his joint training Ph.D. from the University of Arizona, USA, and Nankai University, China, in 2009. His current research interests include nonlinear optics, phononics and acoustics metasurfaces, and subwavelength electromagnetics.